A Surface to Exosphere Non-Orographic Gravity Wave Parameterization for the Mars Planetary Climate Model

Jiandong Liu, Ehouarn Millour, François Forget, Gabriella Gilli, François Lott, Deborah Bardet, Francisco González Galindo, Antoine Bierjon, Joseph Naar, Antoine Martinez, et al.

HAL Id: hal-04191644

https://hal.sorbonne-universite.fr/hal-04191644v1

Submitted on 30 Aug 2023

A Surface to Exosphere Non-Orographic Gravity Wave Parameterization for the Mars Planetary Climate Model

Jiandong Liu[1,2], Ehouarn Millour[1], François Forget[1], Gabriella Gilli[3], François Lott[1], Deborah Bardet[4], Francisco González Galindo[3], Antoine Bierjon[1], Joseph Naar[1], Antoine Martinez[1], Sébastien Lebonnois[1], Siteng Fan[1], Thomas Pierron[1], and Romain Vandemeulebrouck[1]

[1]LMD/IPSL, École Polytechnique, ENS, Institut Polytechnique de Paris, CNRS, Sorbonne Université, Université PSL, Paris, France, [2]Nanjing University of Information Science and Technology, Nanjing, China, [3]Instituto de Astrofisica de Andalucia, Granada, Spain, [4]School of Physics and Astronomy, University of Leicester, Leicester, UK

Abstract In this paper, the non-orographic gravity waves (GW) parameterization of the Mars Planetary Climate Model (PCM) previously implemented by Gilli et al. (2020, https://doi.org/10.1029/2018JE005873) is revisited and extended to the exobase (∼250 km). The simulations performed with the new scheme correct some known biases in the modeled thermal tide amplitudes and polar warming, improving the agreement with Mars Climate Sounder (MCS) observed thermal structures and tides below ∼100 km. Additionally, we find that the simulated densities above 150 km are compatible with NGIMS (Neutral Gas and Ion Mass Spectrometer) measured abundances. Large drag depositions ranging up to >∼950 m s^{-1} sol^{-1} are induced at altitude of 90–170 km due to the wave saturation (breaking) and depletion, leading to winds damped to magnitudes of ∼150–225 and ∼80 m s^{-1} in the zonal and meridional directions, respectively. Resulting temperature variations are ∼±10–30 K or 5%–10% at most latitudes except in the polar regions (where they can reach ∼±30–60 K). The results indicate that non-orographic GW play a significant role in the dynamics of the middle-upper atmosphere of Mars via the induced transfer of momentum and energy from the lower atmosphere.

Plain Language Summary Atmospheric gravity (buoyancy) waves are oscillations that result from flows over topography (orographic gravity waves (GW)) or perturbations caused by convective forcing, front systems, and jet streams (non-orographic GW). In this paper, we model non-orographic GW as a Gaussian wave packet, which is the sum of several monochromatic waves of random wavenumbers and frequencies. The wave packets are launched vertically from low altitudes (∼6 km), where the mean Mars Planetary Boundary Layer is located. We reproduce several features of the thermal structure and tides observed by the MCS by implementing our scheme to the Mars PCM. The scheme has a strong effect on the model's wind fields above an altitude of 35–40 km, transporting momentum from the source layers to higher layers, and even up to the thermosphere (altitude >∼100 km). The temperature and density variations generated by the scheme are comparable to the observations made by the Neutral Gas and Ion Mass Spectrometer. Our results demonstrate that non-orographic GW play a crucial role in the momentum-energy transport that affects the dynamics of the middle and upper atmosphere of Mars.

1. Introduction

The Martian atmosphere is the host of small-scale vertical fluctuations that have been observed by multiple Martian orbiters (England et al., 2017; Fritts et al., 2006; Mahaffy et al., 2015b; Siddle et al., 2019; Starichenko et al., 2021; Vals et al., 2019; Yiğit et al., 2015). Several studies (Medvedev et al., 2011; Roeten et al., 2022; Yiğit et al., 2015) demonstrated that including a functional surface-to-exosphere non-orographic gravity waves (GW) parametrization is needed to represent and account for these small-scale variations in Mars General Circulation Models (GCM). The gravity wave schemes used in the Mars Planetary Climate Model, or Mars PCM (formerly know as the LMD Mars GCM) include two schemes that were adapted from the LMDZ6 (Hourdin et al., 2020) Earth GCM. The orographic scheme designed by Lott and Miller (1997) was integrated in the earlier Mars PCM version by Forget et al. (1999). The non-orographic scheme made by Lott et al. (2012) was recently implemented by Gilli et al. (2020), but limited to the atmosphere below 100 km. However, observations obtained by recent Mars missions show consistent differences with the current GCMs in terms of thermal structures, tides phases and amplitudes, upper atmospheric winds, etc., suggesting the necessity of improvements in simulating the GWs.

Methodology: Jiandong Liu, Ehouarn Millour, François Forget, Gabriella Gilli, François Lott, Deborah Bardet, Francisco González Galindo, Sébastien Lebonnois, Thomas Pierron, Romain Vandemeulebrouck

Project Administration: François Forget

Resources: Ehouarn Millour, François Forget

Software: Jiandong Liu, Ehouarn Millour, François Forget, Gabriella Gilli, Deborah Bardet, Antoine Bierjon, Siteng Fan, Thomas Pierron, Romain Vandemeulebrouck

Supervision: Ehouarn Millour, François Forget, François Lott

Validation: Jiandong Liu, Siteng Fan, Thomas Pierron, Romain Vandemeulebrouck

Visualization: Jiandong Liu, Antoine Bierjon

Writing – original draft: Jiandong Liu

Writing – review & editing: Jiandong Liu

To address these issues, we revisit and extend the non-orographic GW parameterization into the upper atmosphere, and validate it with observations made by Mars Climate Sounder (MCS) onboard Mars Reconnaissance Orbiter (MRO) and Neutral Gas and Ion Mass Spectrometer (NGIMS) onboard Mars Atmosphere and Volatile EvolutioN (MAVEN).

The non-orographic gravity wave parameterization used in LMDZ6 was proposed by Hines (1997) and Manzini et al. (1997). It is a "globally spectral" scheme, in the sense that it directly addresses the vertical changes in the wave spectrum, a technique which was further improved in Warner and McIntyre (1996), Warner and McIntyre (2001). Alternative schemes sample the spectrum stochastically with a large ensemble of individual harmonics. In Lott et al. (2012); Lott and Guez (2013) it is shown that such "multiwave" scheme manage to better simulate the Earth Quasi-Biennial Oscillation in the lower tropical stratosphere. The scheme was then also implemented in the Venus PCM (formerly known as IPSL Venus GCM) by Gilli et al. (2017).

Although the "multiwave" schemes have a long history (Fritts, 1984; Lindzen, 1981; Medvedev et al., 2011; Yiğit et al., 2008), they were considered too slow numerically until Eckermann (2011) and Lott et al. (2012) proposed to sample the spectrum with individual harmonics whose horizontal wavenumber and phase speed are chosen stochastically. The vertical propagation and saturation of each harmonic is then evaluated by using the Wentzel-Kramers-Brillouin (WKB) approximation, a formalism that satisfies the Eliassen-Palm non-interaction theorem in the adiabatic non-dissipative case. Apart from its stochastic aspect, our parameterization is quite similar to the one made by Yiğit et al. (2008), but with quite different criteria to handle the waves' saturation, dissipation, breaking and evolution (Lott & Guez, 2013; Lott et al., 2012).

GW are detected by various observations at different altitudes in the Martian atmosphere. Drag-derived densities/temperatures during a spacecrafts' entry trajectory yield single sampled thermal profiles (see e.g., Figure 3 of Ferri et al. (2019)). These individual profiles might be less suitable for comparing with GCM simulations since the observations embed weather-induced variations. Nevertheless the observed temperature fluctuations in the 10^0–10^{-2} Pa vertical range ($\sim$60–100 km) clearly depict the saturation and depletion of GW. Below altitudes of 40 km, measurements include atmospheric densities/temperatures by radio occultation (Creasey, Forbes, & Hinson, 2006; Tellmann et al., 2013), O_2 dayglow emissions by spectrometers (Altieri et al., 2012), and MCS measured temperatures (Wright, 2012), in which 2–4 K or 3.5% temperature fluctuations are detected. These GW are mostly related to topography (Angelats i Coll et al., 2005; Creasey, Forbes, & Hinson, 2006; Forget et al., 1999; Miyoshi et al., 2011). In the middle atmosphere, a noteworthy feature is the polar warming, which is influenced by GW-altered circulations (González-Galindo et al., 2009; Wilson, 1997) and was detected by successive early observations by Infrared Thermal Mapping (IRTM) experiment (Jakosky & Martin, 1987), Thermal Emission Spectrometer (Smith et al., 2001), and MCS (McCleese et al., 2007, 2008; Heavens et al., 2020). Some of the middle atmosphere cold pockets are moreover believed to be generated by GW (Spiga et al., 2012). In the lower thermosphere, observations include aerobraking accelerometer-derived densities or temperatures with wave amplitudes of 10%–30% or even $\sim$50% (Creasey, Forbes, & Keating, 2006; Fritts et al., 2006; Liu et al., 2019; Vals et al., 2019), Middle InfraRed (MIR) Atmospheric Chemistry Suite (ACS) measured temperatures with 5%–10% disturbances (Starichenko et al., 2021), Imaging Ultraviolet Spectrograph (IUVS) retrievals with temperature disturbances greater than 20% (Nakagawa et al., 2020), and stellar occultation CO_2 density profiles by Spectroscopy for Investigation of Characteristics of the Atmosphere of Mars (SPICAM) with high variability (Forget et al., 2009). Above 160 km, GW are found in the NGIMS measurements with 7%–20% of amplitude (England et al., 2017; Siddle et al., 2019; Yiğit et al., 2015). The amplitudes of these wave-like perturbations derived by observations thus vary from 2% to 50%, which need to be investigated by a surface-to-exosphere GW scheme.

Most of the orographic GW are saturated below 40–60 km (Angelats i Coll et al., 2005; Forget et al., 1999; Miyoshi et al., 2011), contributing to a maximum warming of $\sim$10 K in the polar region at altitudes of 50–70 km. This is due to the adiabatic heating of the downward branch of the Hadley cell, which is brought closer to the pole by the gravity wave drag on the jet stream. In the tropics, above 30 km, less than $\sim$2–4 K variations are generated by the orographic GW breaking (Figure 9c of Forget et al. (1999) and Figure 1 of Angelats i Coll et al. (2005)). The impact of orographic GW on the middle and upper atmosphere is small (Angelats i Coll et al., 2005). We thus expect the non-orographic GW scheme to reproduce the much larger disturbances observed above 30–40 km.

The non-orographic gravity wave scheme of for example, Yiğit et al. (2008), Medvedev and Yiğit (2012), and Roeten et al. (2022) was extended into the upper atmosphere of Mars, yielding significant wave drag (maximum

of ~950 m s^{-1} sol^{-1}). This was also confirmed by the gravity wave-resolving high-resolution model of Kuroda et al. (2016, 2020). However, difficulties exist for integrating such a surface-to-exosphere scheme into a GCM model and being consistent with observations both below and above the mesopause.

In this paper, we present a surface to upper atmosphere non-orographic gravity wave scheme implemented in the Mars PCM. The scheme is constrained and validated by MCS temperatures below ~100 km as in Gilli et al. (2020). The simulated densities of the upper atmosphere major neutral species (CO_2, N_2, CO, Ar, O) are compared with NGIMS observations for Martian Year (MY) 32 to 35. The derivation of the scheme is formulated in Section 2. The results are in Section 3, which describes the momentum deposition caused by the GW, the wind and circulation responses to the momentum divergences, the comparison with MCS thermal structures and diurnal tides, and the comparison with NGIMS abundances. Conclusions are drawn in Section 4.

2. Formalism of the Scheme

2.1. Model Configurations

The Mars PCM (formerly known as LMD Mars General Climate Model) is a 3-D surface-to-exosphere model. The main physical parametrizations of the lower atmosphere are detailed in Forget et al. (1999) and Pottier et al. (2017), and the upper atmosphere ones in Angelats i Coll et al. (2005) and González-Galindo et al. (2009). Earlier versions of the PCM already included an efficient orographic gravity wave parameterization (Angelats i Coll et al., 2005; Forget et al., 1999; Lott & Miller, 1997). A non-orographic GW scheme validated below thermosphere, in which the magnitude of launched momentum fluxes (~10^{-7} kg m^{-1} s^{-2}) was not constrained by observations, was tested by Gilli et al. (2020). There are however now recent ACS observations (Starichenko et al., 2021) which provide some reliable constraints on the possible range of values of the momentum flux parameter (~10^{-3}–10^{-4} kg m^{-1} s^{-2}).

The focus of this paper is on the revision and extension of our non-orographic gravity wave scheme parametrization to the upper atmosphere. It is worth mentioning here that since the work of Gilli et al. (2020) there have been improvements in the PCM parametrizations related to the dust and water cycles driving the lower atmosphere. We leave aside a thorough description of these (which will be discussed in a dedicated paper) and merely mention here that the main improvement in this version, which we label PCM version 6.0, is a better representation of dust in the atmosphere, including the generation of detached dust layers, and of related atmospheric temperatures.

As a main driver of the Martian climate is the amount of airborne dust in the atmosphere, we present and discuss results obtained with PCM6.0 with dust scenarios from MY29 to MY35, a period which includes the planet encircling global dust storm of MY34 (Montabone et al., 2015, 2020).

2.2. Parameterization of the Non-Orographic Gravity Waves

Non-orographic GW can be triggered by atmospheric convection, front systems, and jet streams in the troposphere (Fritts, 1984; Gilli et al., 2020; Lindzen, 1981; Yiğit et al., 2008), where these perturb the stratified atmosphere, leading to adiabatic oscillations of the air parcels due to the gravity-buoyancy forces (Fritts, 1984; Hines, 1997; Lindzen, 1981).

To evaluate the properties of the waves, we consider GW with intrinsic frequency significantly larger than the Coriolis frequency, a case in which the vertical velocity equation for a single harmonic satisfies the Taylor-Goldstein equation (Fritts, 1984; Lindzen, 1981; Lott & Guez, 2013):

$$\frac{\partial^2 \hat{w}}{\partial z^2} + \left(\underbrace{\frac{|\vec{k}|^2 N^2}{\Omega^2} + \frac{\vec{k}(\vec{u}_{zz} + \vec{u}_z/H)}{\Omega} - \frac{1}{4H^2}}_{Q(z)} \right) \hat{w}(z) = 0. \tag{1}$$

where $\Omega = \vec{k}(c - \bar{u})$ is the intrinsic frequency with Doppler shift (Hines, 1997; Warner & McIntyre, 1996, 2001); c the horizontal wave phase speed, $\bar{u}$ the background winds, and $\vec{k}$ the horizontal wavenumber. $\hat{w}(z)$ is the complex amplitude of an harmonic of the vertical velocity perturbation ($w'(z)$). $N^2 = g/T[dT/dz + g/c_p]$ represents the square of Brunt-Väisälä frequency; g the gravity acceleration of Mars, T the temperature, and c_p the specific

heat capacity (varies with T in the scheme). z is the pseudo-altitude: $z = Hln(P_r/P)$ with P the pressure and P_r the pressure at the reference altitude, and H the atmospheric scale height. $\vec{u}_{zz}$ is $\partial^2 \vec{u}/\partial z^2$ and $\vec{u}_z$ is $\partial \vec{u}/\partial z$.

In most circumstances, $Q(z) \approx |\vec{k}|^2 N^2/\Omega^2$. The solution of Equation 1 depends on the sign of the square of Brunt-Väisälä frequency N^2: the vertical velocity starts to grow exponentially if $N^2 < 0$. In contrast, $N^2 > 0$ leads to a sinusoidal (cosinoidal) wave solution. At the top of the convective cells (where $N^2 = 0$), the PBL (Planetary Boundary Layer) oscillates with time due to the evolution of Brunt-Väisälä frequency.

The wave-like solution of Equation 1 can be used to evaluate the vertical structure of each harmonics above sources and before breaking. More specifically, we consider that at each physical step t (of length δt) the vertical velocity w' is represented by a weighted C_j sum of series of monochromatic waves $\hat{w}_j$, that is, $w' = \sum_{j=1}^{M} C_j \hat{w}_j$, where $\sum_{j=1}^{M} C_j^2 = 1$; $M = 8$ waves are used here to fit the solution (Lott et al., 2012). $\forall j \leq M$, the monochromatic wave $w'_j = \Re\left\{ \hat{w}_j(z)e^{z/2H} e^{i(k_j x + l_j y - \omega_j t)} \right\}$ (Fritts, 1984); $\Re$ the real part of the equation; $\omega = \vec{k}c$ is the absolute frequency. To evaluate the wave w'_j, we impose its amplitude $\hat{w}_j$, horizontal wavenumber k_j and l_j, and phase speed c_j randomly at a given reference (launching) altitude z_r, and then iterate from one model level, z_{ll}, to the next, z_{ll+1}, by a WKB approximation:

$$\hat{w}_j(z_{ll+1}) = \Theta[\Omega(z_{ll+1})\Omega(z_{ll})] \ \ Min\left\{ \hat{w}_j(z_{ll})\sqrt{\frac{m(z_{ll})}{m(z_{ll+1})}}e^{-\frac{\mu m^3}{\rho \Omega}\delta z}, \hat{w}_{j,s} \right\} \tag{2}$$

where Θ is the heavyside function such that $\Theta = 0$ when $\Omega(z_{ll+1}) \times \Omega(z_{ll}) < 0$, which occurs when two adjacent levels dub a critical level. $m(z) = N|\vec{k}|/\Omega$ is the vertical wave number. $|\vec{k}|$ is the amplitude of the horizontal wave number k_j and l_j. μ is the vertical viscosity and $\nu = \mu/\rho$ the kinematic viscosity. $\hat{w}_{j,s}$ is the saturation (breaking) amplitude of a monochromatic wave, which is given by Lindzen (1981) and Lott et al. (2012) as:

$$\hat{w}_{j,s} = \frac{\Omega^2}{|\vec{k}| N}e^{-z/2H}S_c\frac{k^*}{|\vec{k}|} \tag{3}$$

S_c is the saturation parameter. $k^* = \max\left(|\vec{k}_{\min}|, 1/\sqrt{\Delta x \Delta y}\right)$. Δx and Δy are the grid intervals of the model (Lott et al., 2012). The term $e^{-z/2H}$ accounts for the decrease of density with altitude.

Once the waves have built up at the reference altitude, the waves' effects are accounted for by their horizontal momentum flux, that is, Eliassen-Palm (EP) flux. When rotation is neglected, the EP-flux amounts to the vertical flux of horizontal momentum (Eliassen & Palm, 1960), which writes as follows at the launch level (Fritts, 1984; Lindzen, 1981; Lott et al., 2012; Yiğit et al., 2008):

$$\vec{F}_j^{z_r}(k, l, \omega) = \Re\left\{ \rho_r\frac{\vec{\hat{u}}\hat{w}^*}{2} \right\} = \rho_r\frac{\vec{k}}{2|\vec{k}|^2}m(z_r)|\hat{w}_j(z_r)|^2 \tag{4}$$

where ρ_r is the mass density at the reference altitude.

We launch the waves at the average top of the planetary boundary layer (approximated to be at $\sigma = P/P_s = 0.6$, which corresponds to a pseudo-altitude of $z_r \approx 5.8$ km when assuming a surface pressure of 610 Pa and an atmospheric scale height H of 10 km) with stochastic EP-flux. Inserting Equation 2 into Equation 4 yields (Lott & Guez, 2013; Lott et al., 2012),

$$\vec{F}_j^{z_{ll+1}} = \frac{\vec{k}\Omega}{|\vec{k}||\Omega|}\Theta[\Omega(z_{ll+1})\Omega(z_{ll})]Min\left\{ |\vec{F}_j^{z_{ll}}|e^{-2\frac{\mu m^3}{\rho \Omega}\delta z}, \rho_r S_c^2 e^{-\frac{z_{ave}}{H}}\frac{|\Omega|^3 k^{*2}}{2N|\vec{k}|^4} \right\} \tag{5}$$

We use k_{min} to replace k^* in Equation 5 to make the saturation amplitude more tunable (De la Cámara et al., 2014). Thus we update the EP-flux by iteration loop from layer z_{ll} to z_{ll+1}, in which $\delta z = z_{ll+1} - z_{ll}$ and $z_{ave} = (z_{ll} + z_{ll+1})/2$, respectively.

The drag tendency caused by the waves is given by $-dF/\rho dz = -\frac{1}{\rho}d\rho\vec{\hat{u}}\hat{w}^*/dz$. Once the drag tendency is evaluated, we use Auto Regression of order one (AR1) to average the drags on the winds and update the winds tendencies between physical time steps t and $t + \delta t$ (Lott et al., 2012; Lott & Guez, 2013),

Table 1
Tunable Parameters of the Scheme

Parameters	$F_{max}^{z_r}$(kgm^{-1}s^{-2})	S_C[a]	μ (m^2 s^{-1})	k_{max} (m^{-1})	k_{min} (m^{-1})	c_{max} (m s^{-1})	$z_r|\sigma$[b] (km|Pa/Pa)	Model top (pseudo altitude) (km)
Gilli et al. (2020)	7×10^{-7}	1.0	1×10^{-3}	7×10^{-4}	2×10^{-5}	30	8|0.4	~120
PCM5.0[c]	5×10^{-4}	1.5	7×10^{-2}	1×10^{-4}	7×10^{-6}	50	5.8|0.6	~250
PCM6.0	5×10^{-4}	1.5	7×10^{-2}	1×10^{-4}	7×10^{-6}	u_{z_r}[d]	5.8|0.6	~250
Ranges	$[10^{-4}, 10^{-3}]$	[0.5, 2]	$[10^{-3}, 10^{-1}]$	$\sim 10^{-4}$	$[10^{-7}, 10^{-5}]$	<80	[1, 20]|[1, 0.16]	

[a]S_C is dimensionless. [b]$\sigma = p/p_s$. [c]Results are not shown in this paper (setup overall similar to Gilli et al. (2020) but extended into the thermosphere). [d]u_{z_r} the zonal wind amplitude at reference level z_r.

$$\left(\frac{\partial \vec{u}}{\partial t}\right)_{GW}^{t+\delta t} = \frac{\delta t}{\Delta t} \frac{1}{M} \sum_{j=1}^{M} \frac{1}{\rho} \frac{dF_j}{dz} + \frac{\Delta t - \delta t}{\Delta t} \left(\frac{\partial \vec{u}}{\partial t}\right)_{GW}^{t} \tag{6}$$

Thus we have $C_j^2 = \left(\frac{\Delta t - \delta t}{\Delta t}\right)^p \frac{\delta t}{M \Delta t}$, where $p = \lfloor (j-1)/M \rfloor$ is an integer. Δt is the life cycle of the non-orographic GW, which is approximately 24 hr or 1 sol (Gilli et al., 2020; Lott et al., 2012). Note that the gravity wave-induced drags are averaged within each call of the routine ($M = 8$ waves launched each δt) and accumulated over the typical life cycle of the waves Δt, which means that about $M\Delta t/\delta t$ harmonics represent the entire spectrum, a number that easily is of the order of 10^3. This excellent spectral resolution at a small numerical cost ($M = 8$ waves are quite fast to evaluate each δt) is one of the benefit of the scheme.

2.3. Tunable Parameters of the Scheme

In order to fine-tune the scheme, the PCM simulations were first validated with MCS temperatures below 100 km, and second compared with NGIMS-measured abundances of neutral species (CO_2, N_2, Ar, CO, and O) in the upper atmosphere (above 150 km). Our tuning requirements are the following: (a) the tunable parameters must have clear physical definitions and the values shall lie within the scope of the related physical process and observations (when possible). (b) the thermal structure/tides of the model with non-orographic GW turned on should match the MCS observations. (c) the scheme should not be sensitive to the value of the physical time step.

The scheme has seven tunable parameters (Table 1). The $F^{z_r} \in \left(0, F_{max}^{z_r}\right)$, $|\vec{k}| \in (k_{min}, k_{max}$, and $c \in (1, c_{max})$ are respectively stochastic truncation values for the EP-flux at reference altitude, horizontal wave number, and phase speed of the GW, which account for the spectral properties of the waves. S_C is a dimensionless factor that governs the amplitude of the saturated monochromatic wave; μ is the viscosity that damps the wave amplitudes at model upper levels; z_r is the altitude/level where the upwards propagating waves are launched.

Where should the EP-flux be launched from? As suggested by Equation 1, the source of the convective non-orographic GW is located just above the PBL where the squared Brunt–Väisälä frequency N^2 changes signs (from negative to positive). However the Mars PBL has strong diurnal variations and therefore the launch altitude of the EP-flux is expected to vary from several meters to 10 km (Petrosyan et al., 2011). In the previous versions of the Mars PCM (Gilli et al., 2020) the wave packets were launched at a fixed pressure level, representative of where the average PBL is located. In the present version, we launch the waves at $\sigma = P/P_s = 0.6$, which is roughly the average altitude of the PBL. Note that the scheme was also tested with launched EP-fluxes at varying altitudes (following the diurnal cycle of the PBL), but such a change in hypotheses induced a significant re-tuning of the scheme which was not pursued here.

We transfer the EP-flux from a level to the next following Equation 5, in which the maximum EP-flux $|\vec{F}_{max}^{z_r}|$ at reference (launch) level z_r needs to be predetermined. As defined by Equation 4, $|\vec{F}_{max}^{z_r}|$ depends on the density ρ_r and the real part of product of $\vec{u}$ and $\hat{w}^*$ at z_r. This term can be 10^{-4} or even 10^{-3} kg m^{-1} s^{-2} on Mars as suggested by Trace Gas Orbiter (TGO) ACS observations (Starichenko et al., 2021), in which the EP-flux is deduced from temperature perturbations by assuming that the average horizontal wavelength of the GW is 300 km.

The horizontal wavenumber is chosen as $\max(k_{min}, k^*) < |\vec{k}| < k_{max}$ stochastically, with $|\vec{k}| = 2\pi/\lambda$; λ the horizontal wavelength. We have replaced the k^* with k_{min} in Equation 5 to make the EP-flux saturation amplitude more tunable (De la Cámara et al., 2014). The amplitude of the horizontal wave number should fulfill the relation

$k* < |k| < k_s$, where $k_s = N/\bar{u}_r$ with N the Brunt–Väisälä frequency and $\bar{u}_r$ zonal wind at the reference level (Lott et al., 2012).

We have set the maximum phase speed c_{max} to the value of zonal wind velocity at launch level, following Lindzen (1981), which makes c_{max} vary with location. The saturation parameter S_C can modulate the saturation EP-flux amplitude by a factor of 1–2. The viscosity μ or kinematic viscosity $\nu = \mu/\rho$ is a damping factor that controls the dissipation of the waves in the higher levels of the model.

2.4. Determining the Values of Tunable Parameters

After ∼100 simulation runs with PCM6.0 dust-water cycle from MY29 to MY35, a set of optimal tunable parameters was obtained based on the tuning strategy described previously. Wide ranges of the parameters have been tested based on Lott et al. (2012) and Lott and Guez (2013), and Gilli et al. (2020) and observational constraints (e.g., Lindzen, 1981; Starichenko et al., 2021).

The identified optimal parameter values and explored ranges are listed in Table 1. The scheme is not very sensitive to S_C and z_r (when z_r is assumed constant and globally homogeneous), and we therefore use values which are of the order of the averages of those suggested by Lott et al. (2012) and Gilli et al. (2020). The maximum phase speed of the waves should be at the magnitude of the background zonal wind according to Lindzen (1981). Parameter μ controls the altitude above which the EP-flux is reduced by dissipation. We set $\mu = 0.07$, which makes the damping layer lie above 120–150 km, where the wave-induced drags are at their maximum (Yiğit & Medvedev, 2017). Note that there is currently a lack of observational constraints for this parameter. The value of $F_{max}^{z_r}$ is compatible with the ACS estimation (Starichenko et al., 2021), which is three order of magnitude higher than Gilli et al. (2020). In order to launch such a quantity of EP-flux at z_r, k_{min} has to be set to 7×10^{-6} m^{-1}, which corresponds to $\lambda_{max} = 1{,}000$ km of maximum horizontal wavelength $\left(\lambda_{max} \approx 2\pi\sqrt{\Delta x^2 + \Delta y^2}\right)$. k_{max} is set to 1×10^{-4} m^{-1}, which implies $\lambda_{min} = 60$ km. Using shorter wavelengths of ∼10 km as in Gilli et al. (2020) leads to individual wave packet occupying a single model grid box ($\Delta x \times \Delta y$) in the polar region, which would not be appropriate (Lott et al., 2012).

The waves' phase speeds c are chosen randomly in $(1, c_{max})$, that is, each individual harmonic has a different phase speed. In PCM 6.0, waves are launched with a varying maximum phase speed c_{max} equal to the background zonal winds u_{z_r} at launch altitude (Lindzen, 1981) rather than a constant value as in PCM5.0. This makes the PCM6.0 wave packets inherently representing a location-dependent spectrum. The distribution of the EP-flux in version 6 has more complex latitudinal variations, which is a better and more accurate representation of the waves' convective nature (Petrosyan et al., 2011).

3. Results and Discussions

3.1. Waves Momentum Deposition

The evolution, saturation (breaking) and depletion (dissipated by $\nu = \mu/\rho$) of non-orographic GW' EP-flux in the vertical direction depends on the prevailing atmospheric state, especially on the background wind and density as implied by Equation 5. On Mars, the spatial distributions of dust and water vapor/ice are the main driver of the state of the atmosphere. As discussed previously there have been some updates in dedicated parametrizations since Gilli et al. (2020) (a configuration also known as PCM version 5.0) leading to improvements in the dust and water cycles (PCM version 6.0) and resulting modeled background atmosphere states. But this change will naturally in turn affect the saturation (breaking) and dissipation of the waves. We hence choose to focus in this paper on PCM6.0 results only, leaving aside the comparison between two PCM version modeled dust and water cycles (to be detailed in a dedicated paper).

The zonal EP-flux and corresponding drags are shown in Figure 1. The meridional component is negligible and thus is not shown. As mentioned by Gilli et al. (2020), the EP-flux and divergence of the flux, that is, drag, deposit mostly on zonal wind in our parameterization due to relative smaller meridional wind amplitudes at the launch level and therefore limits the EP-flux evolution in this direction. The propagation direction of the EP-flux depends on the background winds, where eastwards zonal winds leads to a downward momentum flux and vice versa as shown in the theoretical work of Eliassen and Palm (1960) (see Equation 10.12 therein). The dusty season (which comprises in part the Solar longitudes (Ls) 240°–270°, see Figure 1b) shows in average a
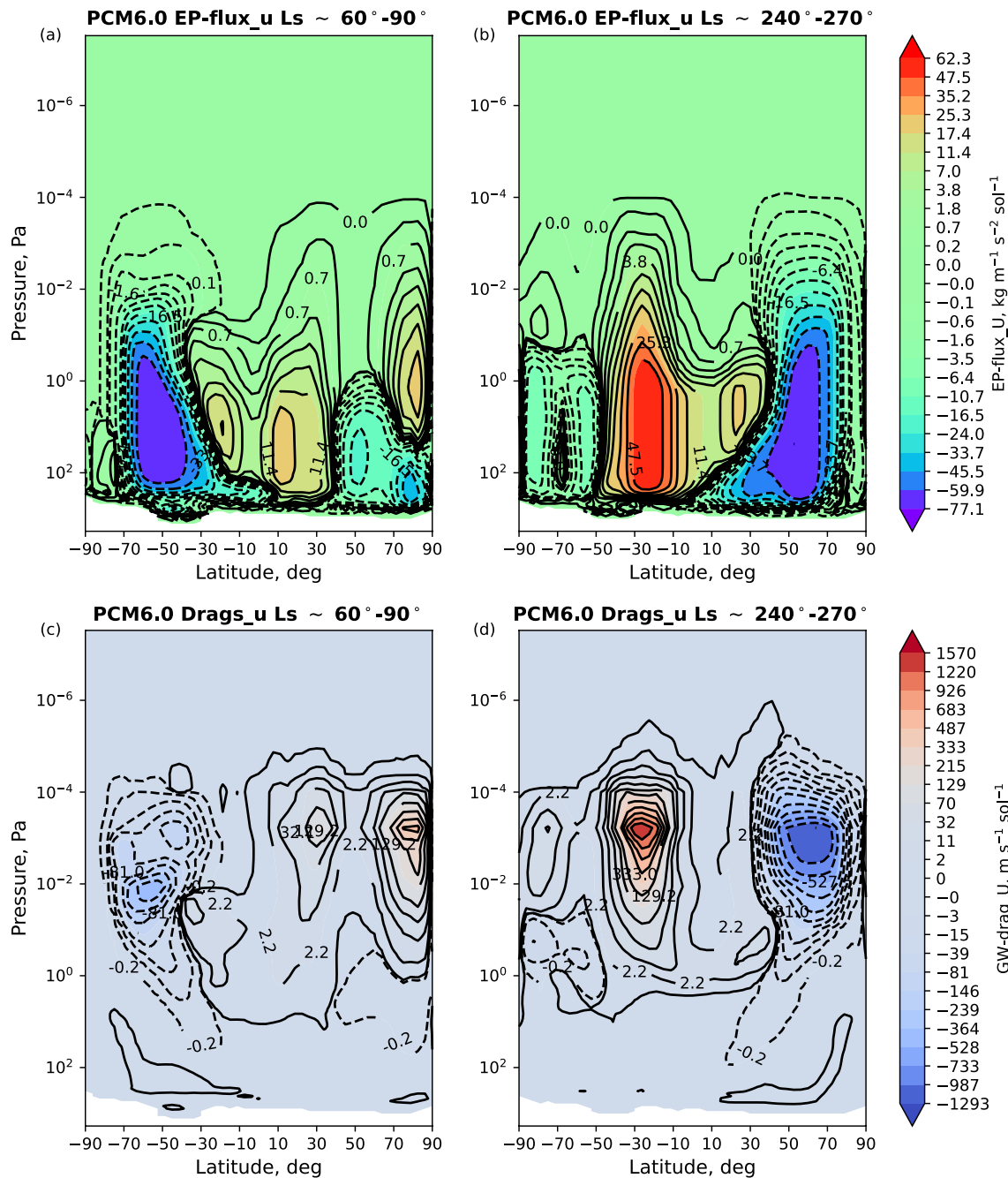
Figure 1. Monthly averaged zonal-averaged gravity wave EP-flux (upper panels) and momentum divergence $((1/\rho)d(\rho u'w')/dz$, that is, drags; lower panels) for Ls 60°–90° (a, c) and Ls 240°–270° (b, d) of MY29. Most of the EP-fluxes are dissipated below 10^{-2} Pa during Ls 60°–90° (a) and 7×10^{-3} Pa during Ls 240°–270° (b), causing huge drag depositions (maximum of $\sim$>950 m s^{-1} sol^{-1}) between $\sim 10^{-1}$ Pa and 10^{-4} Pa (c, d). Note that the intervals of the contour-lines are non-linear.

$\sim$10–20 kg m^{-1} s^{-2} sol^{-1} stronger EP-flux deposition and 10–20 km higher saturation/depletion altitude in the middle atmosphere than the clear sky season (which comprises in part Ls 60°–90°, see Figure 1a) at 45°S–10°S and 30°N–70°N. This leads to more momentum divergences and higher drag deposition altitudes than the clear sky season at the same latitudes (Figures 1c to 1d). In contrast, the clear sky season has a strong EP-flux distribution at 70°S–30°S, causing a strong drag deposition ($\sim$−80 to −360 m s^{-1} sol^{-1}) at the level of 10^{-2} Pa in that region.

Most of the EP-fluxes are saturated below 10^{-2} Pa ($\sim$100 km), and secondary EP-fluxes are generated above these pressure levels (Figures 1a and 1b). Furthermore, most of the fluxes are dissipated by the kinematic viscosity

and depleted below 10^{-4} Pa ($\sim$150–170 km) before reaching the model top (there are still some low-magnitude (10^{-2}–10^{-3} kg m^{-1} s^{-1} sol^{-1}) EP-fluxes, not visible in Figure 1, that can reach beyond 10^{-7} Pa or even higher levels). This makes the (absolute) momentum divergence (Figures 1c and 1d) reach its maximum of >$\sim$950 m s^{-1} sol^{-1} between 90 ($\sim$10^{-1} Pa) and 180 km ($\sim$10^{-5} Pa).

The depletion altitude of the waves is increased by 15–25 km on average during the dusty season compared to the clear sky season, resulting in stronger energy deposition in the thermosphere (Figures 1c and 1d). The dusty season maximum of momentum divergences even reaches $\sim$950–1,600 m s^{-1} sol^{-1} at altitudes of 100–170 km. The dust storms and corresponding overall higher airborne dust loading cause atmospheric expansion, increasing the atmospheric density both in lower atmosphere and upper layers (Benna et al., 2019; Kuroda et al., 2020), which decreases the factor $\nu = \mu/\rho$ and thus prevents the waves from saturation (breaking) and depletion. This favors the waves propagating to higher altitudes, causing stronger drag depositions there due to thinner atmospheric density. An increase of the GW breaking altitude of 15–20 km during dust storm is also observed by Yiğit et al. (2021) using NGIMS CO$_2$ abundance and by Liu et al. (2019) with accelerometer-derived density.

3.2. Impacts on Winds

The momentum divergence directly acts on the wind tendency. The growth, saturation (breaking), and depletion of the EP-flux thus influence wind gradients dramatically (Figures 2 and 3). We evaluated the non-orographic GW' impacts on the winds by comparing between model simulations without (Figures 2a and 2d) and with (Figures 2b and 2e) the scheme activated. The differences are evaluated as $\bar{u}_{GW\,on} - \bar{u}_{GW\,off}$ and $\bar{v}_{GW\,on} - \bar{v}_{GW\,off}$ (Figures 2c and 2f), respectively.

The GW' effects on the winds during clear sky season are shown in Figure 2. The zonal wind starts to be altered by the GW at 10° Pa (above $\sim$35–40 km, Figures 2b and 2c), where some of the wave packets start to saturate (break) and deplete due to the sign change of Ω (i.e., $|c - \bar{u}| = 0$). Below this altitude, the atmosphere is thick enough to contain and absorb the energy deposition of the waves. The wave drag influence on the meridional winds below 10^{-1} Pa (above $\sim$80 km) (Figures 2e and 2f) is in line with the maximum of horizontal momentum divergences illustrated in Figure 1. During the clear sky season (Figures 2c–2f), the changes of zonal and meridional winds induced by the wave drags' depositions can respectively reach amplitudes of $\pm$125 m s^{-1} and $\pm$60 m s^{-1}.

By comparing with the simulations without the GW (Figures 2a and 2d), we find that in most cases the winds are damped by the waves. During Ls 60°–90°, the southern hemisphere high latitude eastward zonal winds and southward meridional winds are damped by 50 m s^{-1} and 20 m s^{-1} (Figures 2c and 2f), respectively. The strong momentum deposition at 70°S–30°S and a level of 10^{-2} Pa damps the zonal jets by 100 m s^{-1} in the southern polar region (Figure 2c) and leads to meridional wind reversal there, of an intensity of -10 to -30 m s^{-1} (Figures 2e and 2f).

During the dusty season (Figure 3), the middle to upper atmosphere westward zonal winds are all damped and even reversed by the GW in the northern hemisphere (Figures 3b and 3c). The meridional winds are damped by the waves between $\sim$10^{-1} to $\sim$10^{-4} Pa and accelerated by 10–20 m s^{-1} above $\sim$10^{-4} Pa (Figures 3e and 3f). The GW impact on the winds are stronger during the dusty season than the clear sky season, which is due to the enhanced momentum divergence and the saturation altitude as shown in Figure 1.

3.3. Influences on the Circulations

The impacts of non-orographic GW momentum deposition on the atmospheric circulation are illustrated in Figure 4. The momentum deposition induced by GW saturation and depletion increases the zonal wind gradients in the equatorial region noticeably (subplots (b) and (c) of Figures 2 and 3) and provides stronger momentum to the Mars circulations than without non-orographic GW. In other words, more equatorial absolute angular momentum M is generated due to the increase of the zonal wind gradients (Figure 4, lower panels). This leads to two outcomes: (a) the north-to-south Hadley cell during Ls 60°–90° is strengthened above 80 km, resulting in downward branch brought closer to the southern pole (Figure 4b) and thus correcting the model biases there (Figure 4a). (b) the south-to-north Hadley cell during 240°–270° is weakened above 80 km and a new local counterclockwise circulation is generated at 15°N–35°N and an altitude of 60–70 km. The weakened downward branch of the circulation generates a cooler north polar warming (Figure 4d) than without GW (Figure 4c). Several instruments have
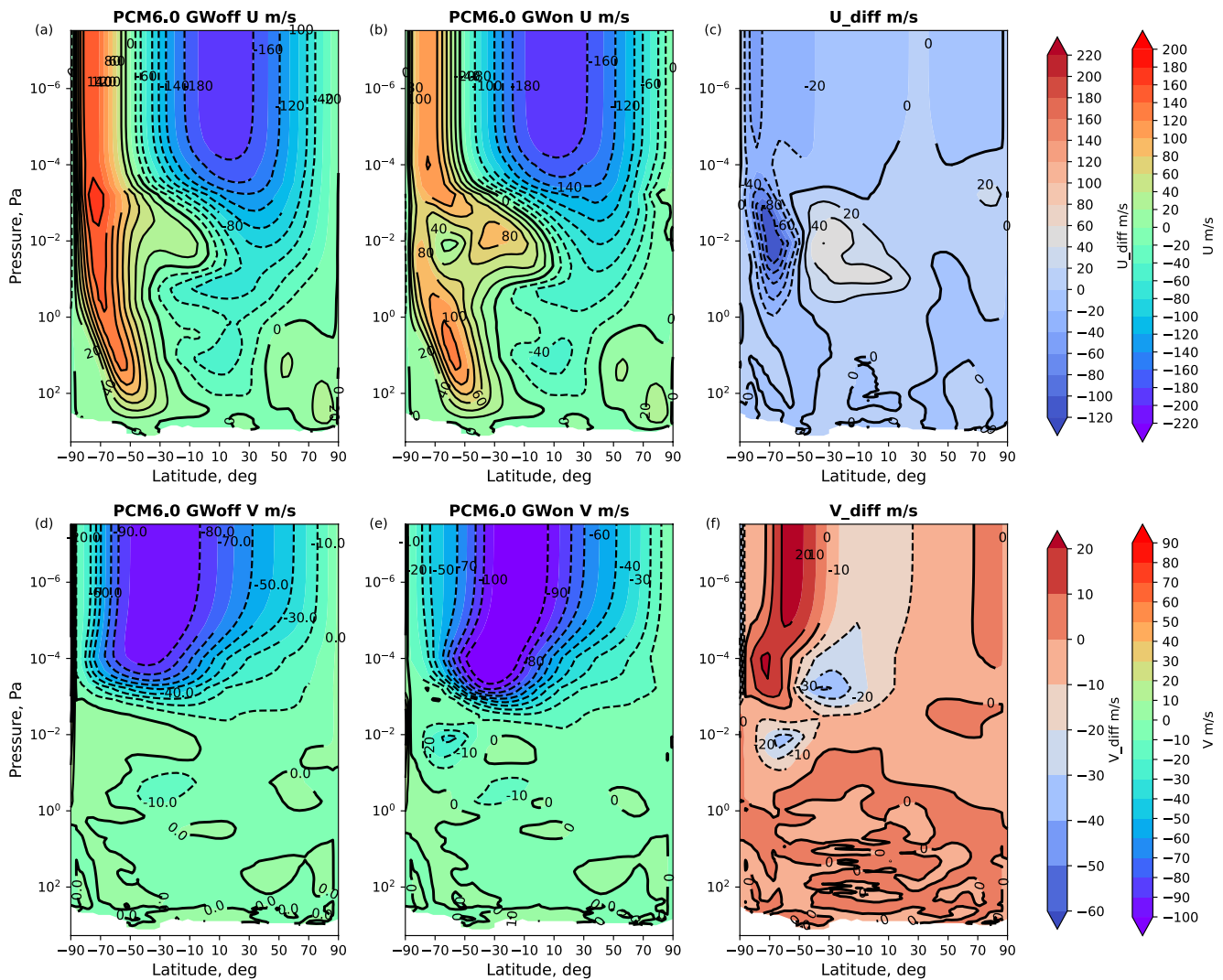
Figure 2. Monthly averaged zonal-averaged winds during the clear sky season Ls 60°–90°, MY29. Unit: m s^{-1}. (Upper) Zonal wind (a) without and (b) with non-orographic GWs; (c) the gravity waves effects, that is, GWon-GWoff. (Lower) Corresponding meridional winds (d, e) and differences (f, i.e., e–d). The zonal (meridional) winds are damped in both eastwards (southwards) and westwards (northwards) directions.

observed the middle atmospheric polar warming (e.g., Jakosky & Martin, 1987; McCleese et al., 2007, 2008, and others; Smith et al., 2001), which is influenced by adiabatic heating of the downward branch of the Hadley cell (Forget et al., 1999; González-Galindo et al., 2009; Medvedev & Yiğit, 2012; Wilson, 1997). The new generated counterclockwise circulation prevents part of the global clockwise cell from going to the north pole, forcing this part of circulation to turn downwards in the equatorial region and thus yielding a moderate middle atmosphere equatorial warming (Figure 4d).

The momentum deposited in the south polar region during clear sky season at pressure of 10^{-2} Pa dampens the zonal wind on the downward Hadley cell (Figures 2b and 2c), for which the absolute angular momentum is decreased there (Figure 4f) compared to the case without GW (Figure 4e). This causes a cell cooling down to 120–135 K in that region (Figure 4b, ~80–120 km; 70°S–30°S). The breaking of waves in the middle atmosphere of the equatorial region generates a zonal wind gradient that pushes the downward branch of the Hadley cell closer to the south pole (Figures 4a and 4b), which improves the thermal structure of the southern polar warming (Figure 4b). Just above the cold cell (located around 80°S to 50°S latitudes), the downward streamlines at altitudes of 120–150 km are enforced by the GW, resulting in thermal structure changes (the warming tongue in Figure 4b) at these altitudes.

Figure 4d shows that new circulation patterns can be generated by GW during the dusty season. In the middle atmosphere equatorial region, GW induce zonal winds gradients (Figure 3c) and correspondingly enhance
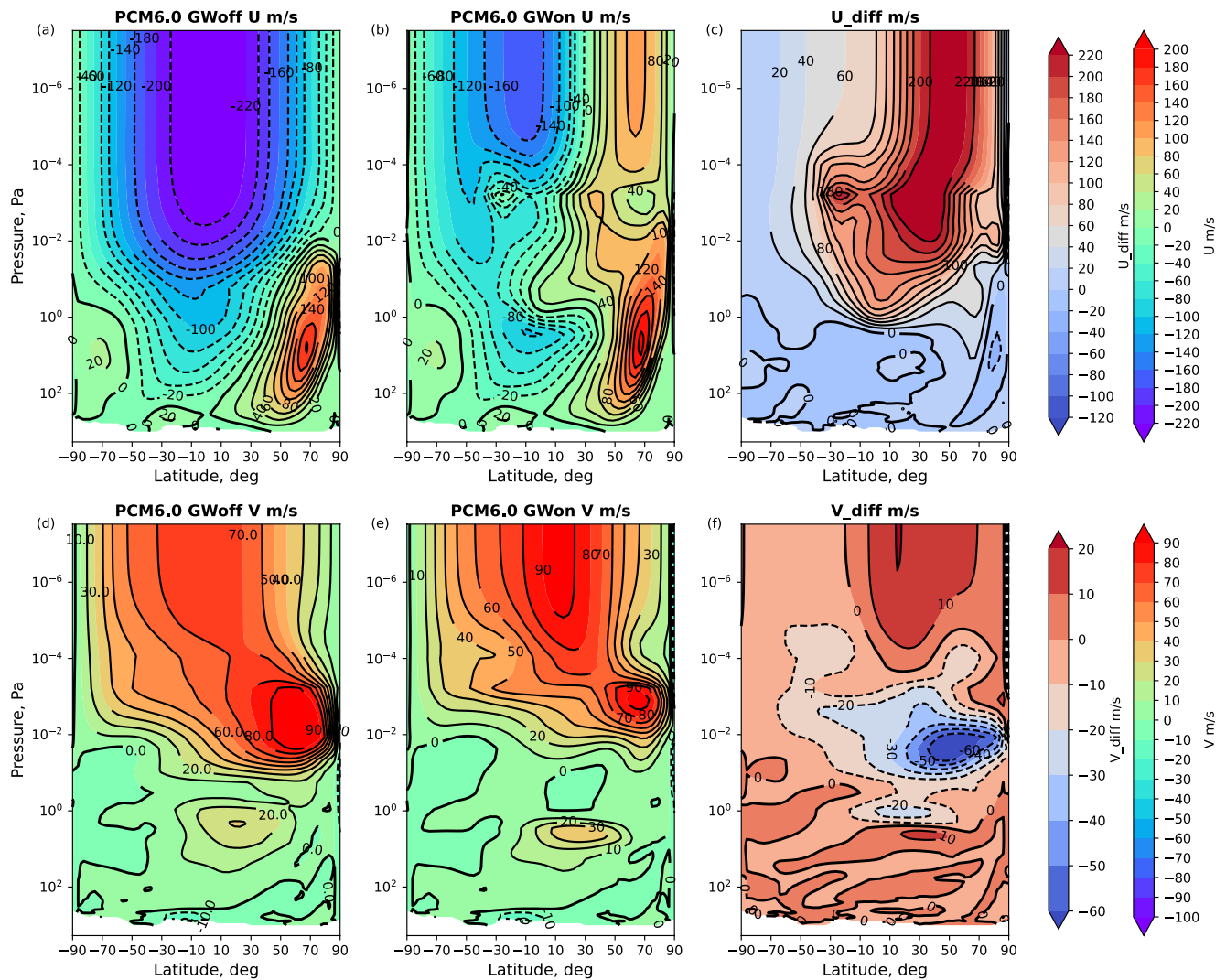
Figure 3. Same as Figure 2 but for the dusty season Ls 240°–270°, MY29. Zonal wind reversals can be generated by the gravity waves during this season, especially in the northern hemisphere.

absolute angular momentum (Figure 4h). This generates a new small counter-rotating cell (Figure 4d) disturbing the global south-to-north pole one, causing some warming there (above ∼60–100 km) and a tilt cool trough extending from 30°N to 90°N at altitudes of 70–150 km.

The temperature changes in the 100–150 km region due to the changes in circulation have a significant impact on the upper atmosphere above (Figures 4b and 4d). Enhanced absolute angular momentum strengthens the counterclockwise circulation (north-to-south) both locally and globally and weakens for the clockwise circulation (south-to-north).

3.4. Comparisons With MCS Temperatures

The tuning strategy is to constrain the model temperatures below 100 km with MCS observations to derive optimal parameters values (listed in Table 1) and then compare with NGIMS densities in the upper atmosphere.

In this section, we validate and constrain the parametrization using MCS temperatures. MCS is an infrared radiometer onboard MRO with nine channels (McCleese et al., 2007), which can operate both in limb and nadir geometry, and provides continuous and global thermal observations for Mars (Kleinböhl et al., 2017). The temperatures are retrieved from three channels that cover the wavelength of the 15 μm CO_2 absorption band with
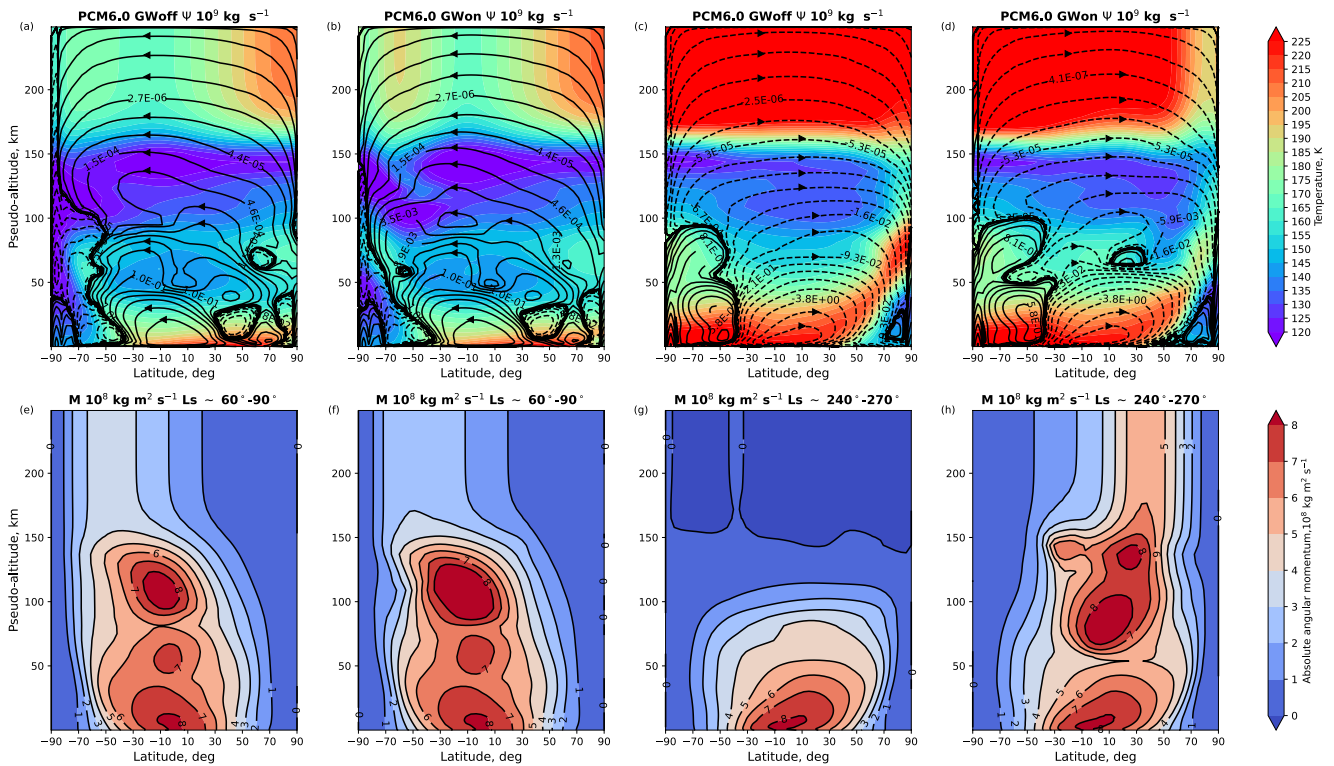
Figure 4. Non-orographic GWs' effects on the Martian circulation. (Upper panels) Meridional mass stream function Ψ, 10^9 kg s^{-1} (temperatures in background, K); (a) reference run, (b) simulation with gravity waves on during Ls 60°–90°; (c) and (d) for dusty season (Ls 240°–270°, MY29.) (Lower panels) same as upper panels but for absolute angular momentum (10^8 kg m^2 s^{-1}). The vertical axes are in pseudo-altitude. Note that the intervals of contour lines of Ψ are non-linear.

~10 K accuracy over altitudes of 10–100 km (Kleinböhl et al., 2009, 2017). For our comparisons, the temperature profiles were binned over 5 degrees of solar Longitude (Ls) (Liu et al., 2023). The profiles are reliable for altitudes above 10 km (McCleese et al., 2008, 2010). MRO sun-synchronous polar orbit enables two local times of measurement, with mean solar local times of measurement at 3 p.m. ("day") and 3 a.m. ("night") at the equator. Here the investigated thermal structures are those obtained as day-night average (diurnal) temperature and day-night difference (thermal tide signature).

Figure 5 shows Mars thermal structure and thermal tides during the clear sky season as observed by MCS (McCleese et al., 2008) and simulated by PCM6.0. The polar warming feature is influenced by the adiabatic heating of the downward Hadley circulation as shown by Forget et al. (1999). In the PCM simulation without GW, the southern branch of the Hadley cell dives before reaching the south pole (Figure 4a). The PCM simulation with GW generate a polar thermal structure (Figure 5c) compatible with the observed one (Figure 5a), due to the low EP-Flux in the equatorial region (Figure 1a). The parameter $c_{max} = u_r$ setting also limits the amount of momentum launched from the equatorial region. The effect of GW on the clear sky season thermal structure is ~15–45 K in winter high latitudes and polar region and 3–5 K in other regions (for altitudes >40 km).

A quadrupole structure exists in the diurnal thermal tide seen by MCS (Figure 5e) (Lee et al., 2009). A similar structure is reproduced by the model without GW (Figure 5f), however, the amplitude is ~8 K higher and the vertical phase of the structure is 10–15 km higher than the observations. The amplitude of the tide is influenced by GW (Figures 5g and 5h). The vertical phase is however found to be not sensitive to the GW at all.

In the dusty season (Figure 6), apart from a strong polar warming, observations also display a moderate equatorial middle atmospheric warm structure, and a cold trough starting from 1 Pa to 10^{-2} Pa, near the north pole (Figure 6a). This is also the case in the simulation with GW (Figure 6c) but not without (Figure 6b). These two features are thus induced by GW-altered winds or circulations (Figure 4). The equatorial feature and the cold trough are due to the dynamical heating from the altered circulations (Figure 4). The GW' effects on the thermal structure is >~15–55 K in northern latitudes and polar region and 10–15 K elsewhere (for altitudes >40 km).
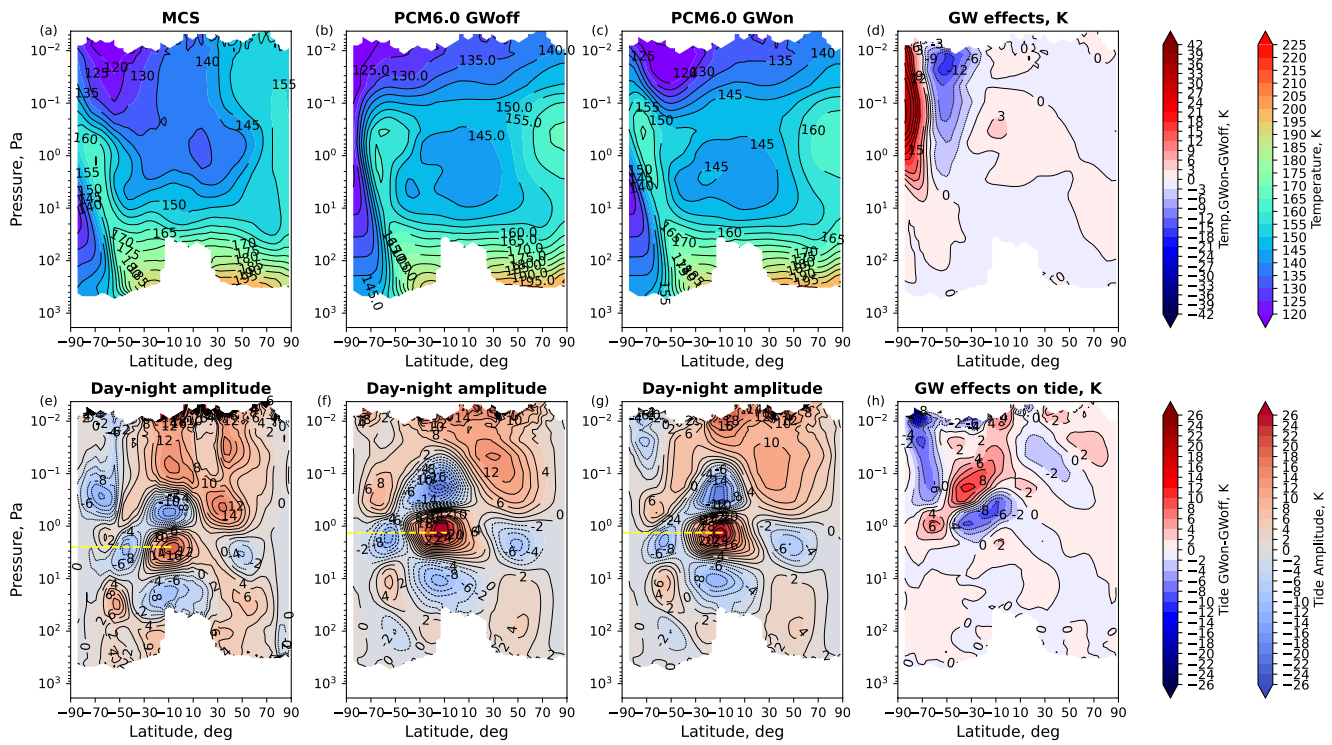
Figure 5. Thermal structure and tides during the clear sky season of MY29. (Upper panels) Monthly mean zonal-averaged Mars atmospheric thermal structure (day/night average). Ls 60°–90°, MY29. (a) Mars Climate Sounder observations, (b) reference simulation (PCM6.0 configuration without gravity wave scheme), (c) simulation with the gravity wave scheme, and (d) gravity waves' effect, that is, (c–b). (Lower panels) same as upper panel but for the diurnal thermal tide (day-night difference). Yellow dashed line indicates the vertical phase of the diurnal thermal tide's local maximum. Displayed altitudes are below 100 km.
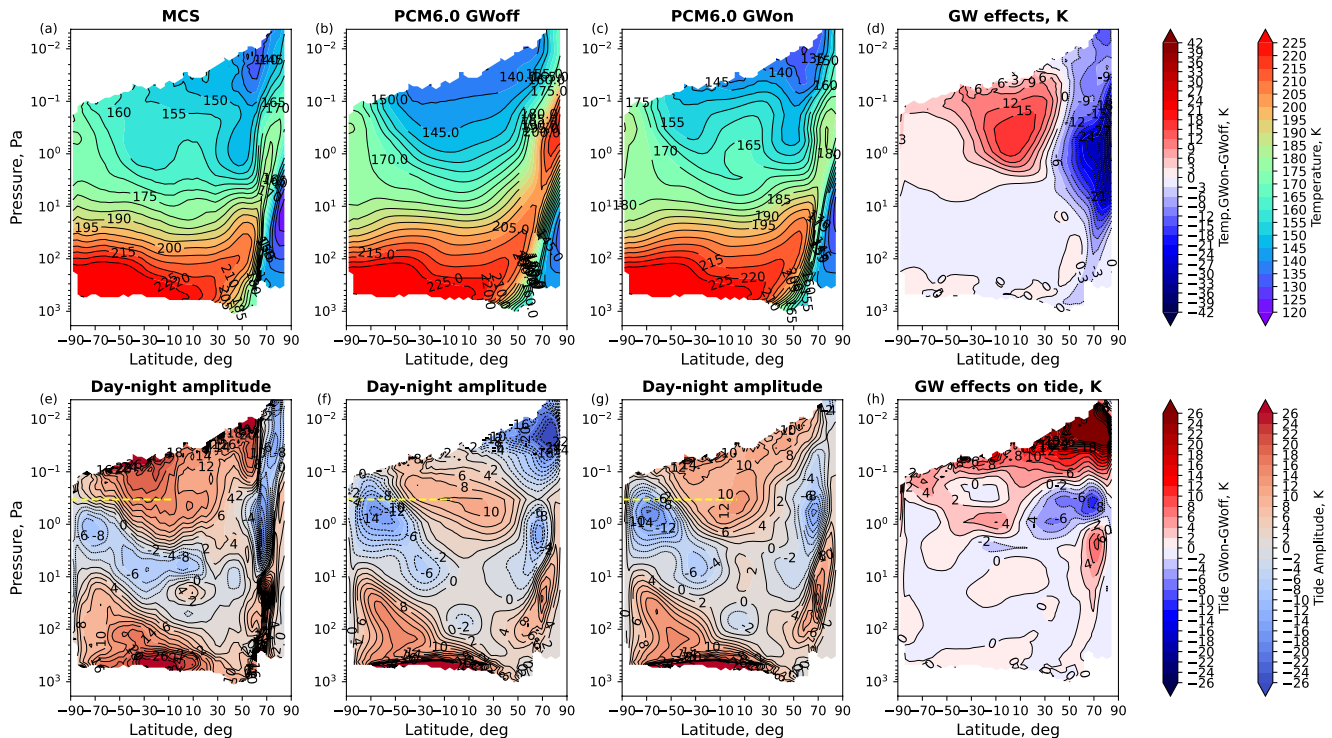

Figure 6. Same as Figure 5 but for the dusty season, Ls 240°–270°, MY29.
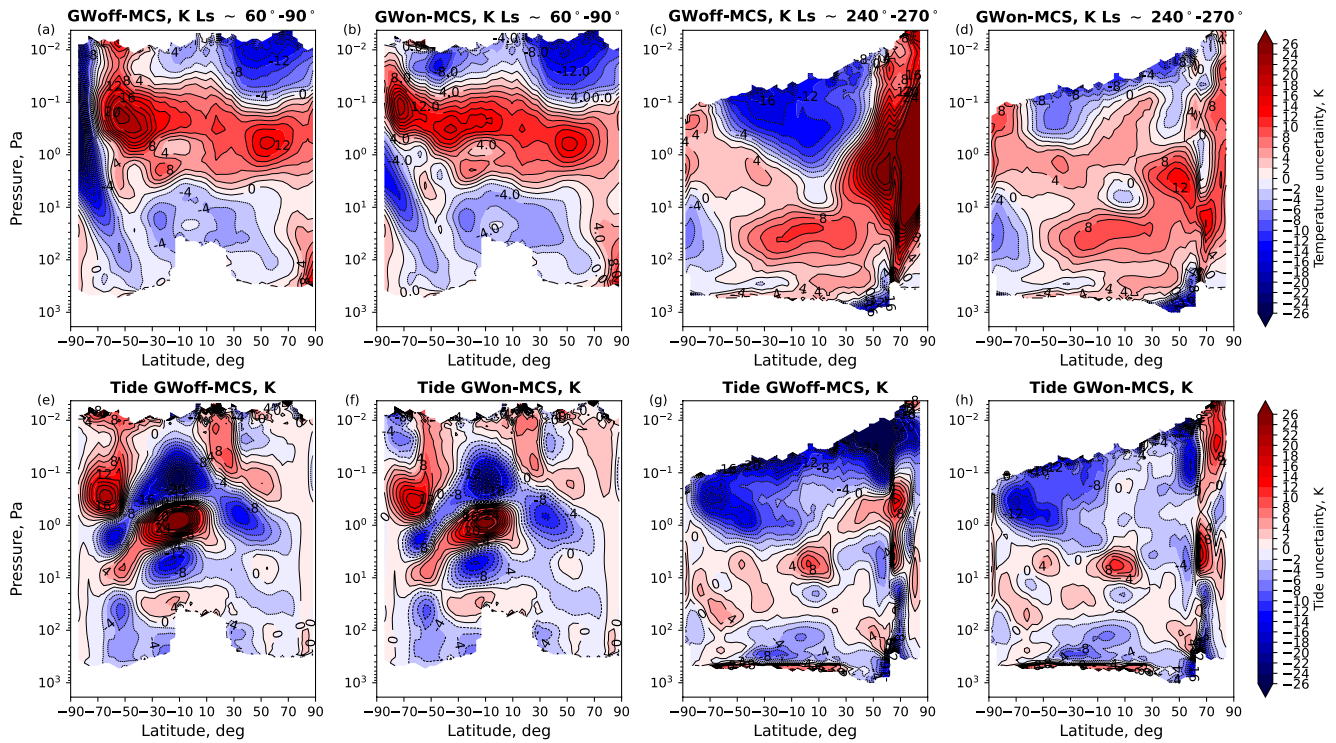
Figure 7. Model difference to Mars Climate Sounder observations (PCM-MCS). (Upper panels) Thermal structure difference, K; (a) GWoff-MCS and (b) GWon-MCS during Ls 60°–90°, MY29; (c) GWoff-MCS and (d) GWon-MCS during dusty seasons Ls 240°–270°, MY29. (Lower panels) same as upper panel but for the difference of diurnal thermal tide.

The diurnal thermal tide is reproduced by PCM6.0 with the gravity wave scheme. The warm spot in equatorial region (latitude: 10°S–30°N; center at altitude 9×10^1 Pa, ~35 km) is caused by the coupling of dust and water cycles and the GW (Figures 6e and 6g). The thermal tidal amplitudes are highly improved by the scheme (Figure 6g), where the triangle-like warming structure observed by MCS (Figure 6e) is recovered by the simulation with the gravity wave scheme (Figure 6g). The large bias of the simulated thermal tide (Figure 6f) produced without the scheme are corrected by the waves effects especially at altitudes of $10^0–10^{-2}$ Pa (Figure 6h).

Figure 7 shows the PCM-MCS differences. The simulation with GW (Figures 7b and 7d) corrects the polar warming in both hemispheric winters systematically compared to the one without the scheme (Figures 7a and 7c). The thermal structure above 10^1 Pa is also overall improved by the GW during the dusty season (Figures 7c and 7d). However, GW have little effect, if not none, on the model's warm bias in the lower atmosphere ($10^2–10^1$ Pa), nor on the global warm layer that arises between $10^0–10^{-1}$ Pa in the clear sky season. Corresponding improvements in amplitudes of diurnal thermal tides can also be seen from lower panels of Figure 7.

3.5. Comparisons With NGIMS Densities

The Neutral Gas and Ion Mass Spectrometer (NGIMS) onboard MAVEN mission has sampled in-situ gas and ion density of the Martian upper atmosphere ever since the spacecraft entered Mars orbit in 2015 (Benna & Lyness, 2014), providing high accuracy records of neutral species densities (e.g., CO_2, Ar, CO, N_2, O etc.) of the Martian upper atmosphere (Mahaffy et al., 2015a, 2015b).

The L2 data set of NASA-PDS (Benna & Lyness, 2014) is used here, as is often the case when studying the Mars upper atmosphere thermal structure and variability thereof (England et al., 2017; Mahaffy et al., 2015b; Siddle et al., 2019; Terada et al., 2017; Vals et al., 2019; Yiğit et al., 2015). Only inbound observations are used in this paper. The spatial distribution of the data is available in England et al. (2017) or Li et al. (2021).

NGIMS-measured neutral densities of CO_2, N_2, Ar, CO, and O (Stone et al., 2018) are compared to model simulations. The selected observations used in this comparison are at an altitude of 180 ± 1 km, start at the MY32
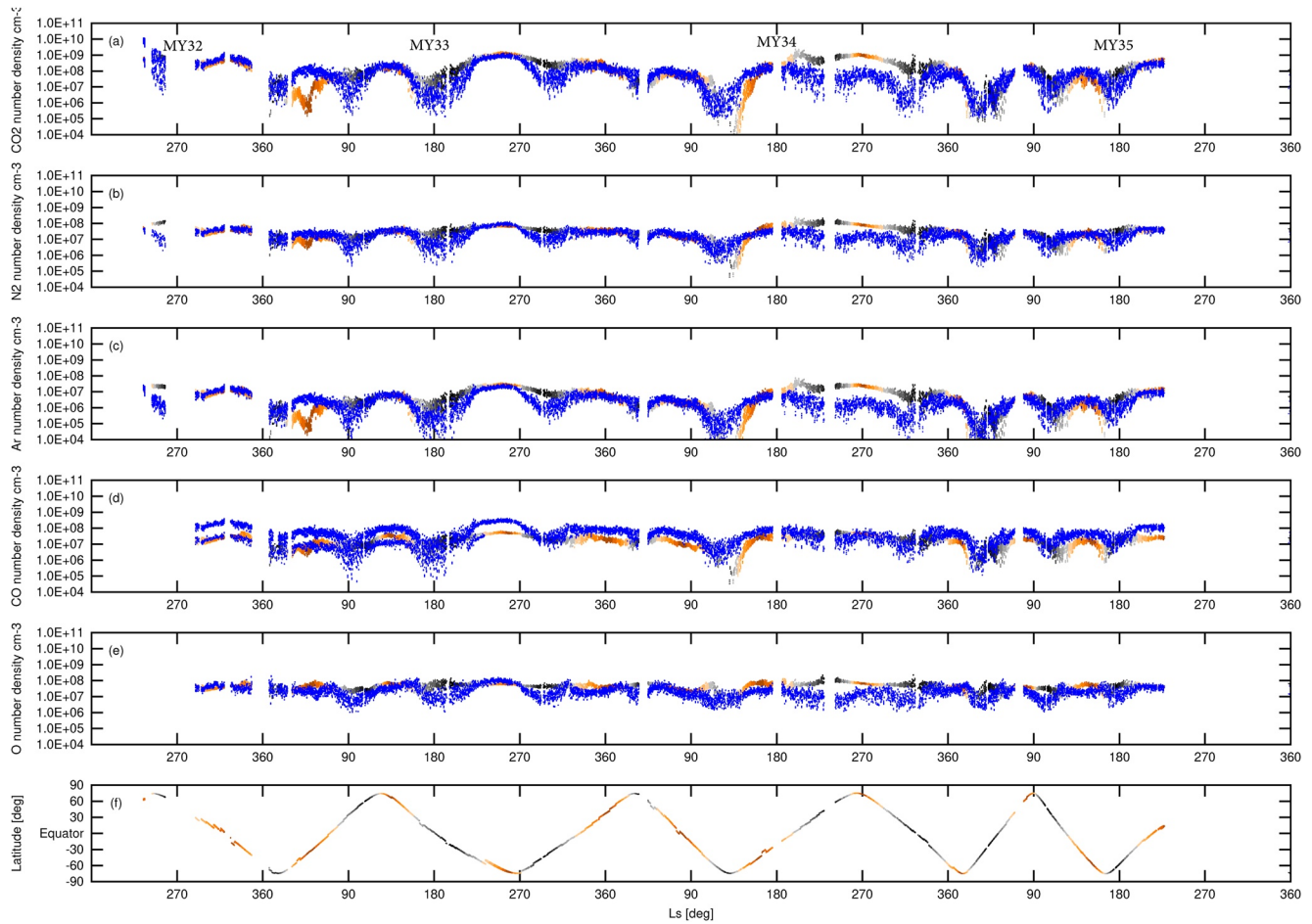
Figure 8. PCM6.0 without gravity waves simulations (gray-brown) and NGIMS retrieved (blue) number densities at the altitude of 180 ± 1 km of (a) CO_2, (b) N_2, (c) Ar, (d) CO, and (e) O, point-to-point comparisons. MY32–MY35. (f) Locations and Local Solar Time of the observations (Ar). The gray(night)-brown(day) cyclic color evolution represent the night-day cycle with dark gray at 24 hr and dark brown at 12 hr.

autumn dust peak (Ls ∼ 216°) and end in MY35 autumn (Ls ∼ 240°). The observational window includes MY34, during which a global dust storm occurred, providing a good opportunity to study the upper atmosphere responses to the dust-GW coupling. We focus on the altitude of 180 km for two reasons: (a) This altitude is 20–30 km higher than the MAVEN average orbital periapsis (150–160 km), where the trajectory is mostly vertical with limited horizontal contributions. (b) The PCM model top can drop below ∼210 km during the polar night, with some potential numerical boundary contributions affecting simulation results. Additionally, in the data there are some cases of two apparent sets of observations (a same orbit with two quite distinct values at each sample point) in CO_2, N_2, Ar (Ls ∼210°–240°, MY32) and CO (Ls ∼290°–360°, MY32; Ls ∼0°–230°, MY33). We do not discuss or elaborate on the reason for these two data sets and merely note that deriving the CO densities is likely subject to disturbance from other atomic mass 28 species, which must be removed to isolate the signal of atmospheric CO (Mahaffy et al., 2015a, 2015b; Stone et al., 2018).

Figure 8 shows the PCM6.0 simulation results without the gravity wave scheme versus the NGIMS abundances. The number density of all species except CO are overestimated by one order of magnitude by the model without GW during night and during the dusty seasons. The model dayside CO_2 number density fits well the observations during MY32, MY33, and MY35 especially during the winter (Ls 270°–360°). However, the dayside CO_2 values are underestimated for the southern hemisphere (latitude 0°S–60°S, Figure 8f) by 2 orders of magnitude (2.E+02 cm^{-3}) during MY33 Ls 30°–60° and MY34 Ls 140°–160° (Figure 8a). This is also the case for N_2 and Ar (Figures 8b and 8c). The densities are globally overestimated during the MY34 global dust storm (Ls 180°–360°), except for CO. As previously mentioned, the CO observations display a split in two incompatible sets (Figure 8d) at the beginning of the retrievals, before remaining only with the set corresponding to higher CO concentrations.
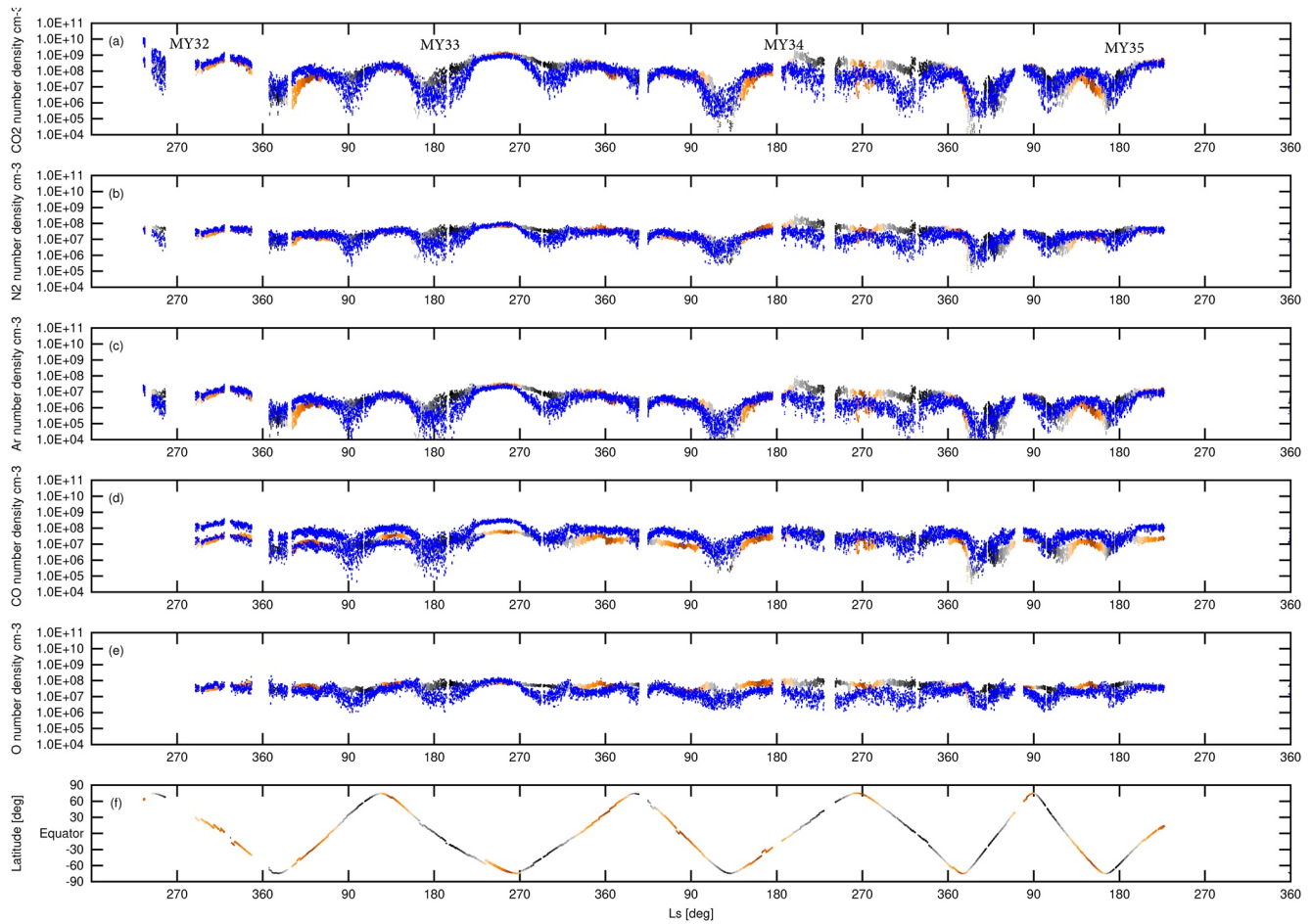
Figure 9. Same as Figure 8 but for PCM6.0 with gravity waves.

The model reasonably represents the average yearly evolution of CO, but would better match with the observation set corresponding to lower CO concentrations. The model also produces a weaker O diurnal cycle than the observations (Figure 8e).

The net effect of the GW in PCM6.0 is to decrease the biases between the simulated and the observed abundances (Figure 9). In these simulations the number densities of all the species decrease during night, compared to the simulations without GW (Figure 8). The large density biases during MY33 Ls 30°–60° and MY34 Ls 140°–160° in the southern hemisphere are corrected by the scheme, which brings simulations much closer to observations (Figures 9a–9d). The O diurnal cycle is not strengthened by the waves (Figure 9e). Overall, adding GW increases the density variability, consistently with the observations (see e.g., MY32 Ls 250°–260° and MY34 Ls 250°–300°, North pole region).

The main driver of the lower atmosphere temperature is airborne dust which in turn has an impact on the GW momentum deposition, closely tying the two. We note that there is systematically a stronger mismatch between PCM6.0 and NGIMS densities during dusty events (e.g., MY32 Ls 250°–260° and MY34 Ls 190°–350° on Figures 8 and 9).

Observations display more spread along altitude and local time than the model both with and without GW, especially during night (Figures 8 and 9). This could be related to some gravity-wave-induced mixing (Lindzen, 1981), not accounted for in the current model.

4. Conclusions

A surface-to-exosphere non-orographic GW scheme is implemented in the Mars PCM by revisiting the parameterization of Gilli et al. (2020). The scheme works consistently from the surface to the exosphere with the

revised parameterization. The simulated results are in better agreement with MCS-observed thermal structure/tides below the upper atmosphere and are compatible with the species abundances (CO_2, N_2, Ar, CO, and O) measured by NGIMS at 180 km. Our main conclusions are the following:

1. Most of the wave packets saturate at altitudes of 80–140 km, with latitudinal variations, due to the change of sign of Ω between two adjacent layers. The eastward zonal winds create downward EP-flux and vice versa below the upper atmosphere (Eliassen & Palm, 1960). The amplitude of the average momentum flux is proportional to the zonal wind amplitude, which can reach up to ± 80 kg m^{-1} s^{-2} sol^{-1} depending on the latitude. The average saturation altitude during the dusty season is 15–20 km higher than for other periods of the year.
2. The drags caused by the saturation (breaking) and the depletion of the waves are maximum ($> \sim \pm 950$ m s^{-1} sol^{-1}) at 90–180 km. This triggers new jets and wind reversals in the upper atmosphere. Dust storms can enhance the altitude of the maximum of drag depositions by one or two scale heights due to the enhanced GW saturation altitude. This has also been noticed by Roeten et al. (2022).
3. The breaking of the waves in the equatorial region induces more wind gradients in the simulated middle atmosphere, which has significant impacts on the Hadley cells: The momentum provided by these wind gradients pushes the downward branches of the circulation closer to the poles, correcting the previous biases in the Hadley cell position during Ls 0°–90° in the model.
4. The upper atmosphere winds are damped (sometimes even reversed) by the momentum transmitted by the GW. The induced meridional and zonal wind variations are respectively up to ± 170 or ± 240 m s^{-1}.
5. The simulated atmospheric temperatures below 100 km are consistent with MCS observations. Several features in the middle atmosphere can now be explained by GW' effects: (a) The Hadley cells are powered by the momentum released from the breaking GW at equatorial middle atmosphere, which means the descending latitude of the downward branch of the circulation is modulated by the waves-induced zonal wind gradients. The adiabatic warming due to compression of the downward branch with the atmosphere generates the polar warming. The amplitude of the polar warming is damped by the GW. (b) The low temperature trough at latitudes 40°–70° (spring at SH and autumn at NH) is confirmed to be generated by GW. This feature is caused by the thermal effects of the damped winds and resulting altered circulations. (c) The moderate warming at the equatorial middle atmosphere is confirmed to be generated by the GW during the dusty season. (d) The amplitudes of the diurnal thermal tides are modulated by the GW. However, the vertical phase of the tides is not influenced by GW.
6. The net effect of the GW is to cool the upper atmosphere (also by Roeten et al. (2022)), which brings the density estimates of the upper atmosphere of the model closer to NGIMS observations.
7. A strong atmospheric dust loading leads to heating and thus expands the atmosphere, resulting in changes of the atmospheric state that guide the saturation altitude of the GW. Thus the vertical phase of the middle atmospheric tides is sensitive to the dust opacity and the tides' amplitude is modulated by the waves.

The model simulations are still missing some variability present in the NGIMS observations of the upper atmosphere, which might be resolved by introducing the GW induced eddy diffusion (mixing) (Lindzen, 1981). Including this effect in the model could be a direction for future work.

Data Availability Statement

The NGIMS densities (Benna & Lyness, 2014) and the temperature profiles for MCS (McCleese & Schofield, 2008) are available at NASA Planetary Data System. The binned MCS temperature (Liu et al., 2023) used in this paper are available in NetCDF format at Mendeley Data. The Mars PCM is freely available from svn.lmd.jussieu.fr/Planeto/trunk. We used revision r2842 for this study and simulation results shown in this paper can be recovered by running it.

References

Altieri, F., Spiga, A., Zasova, L., Bellucci, G., & Bibring, J.-P. (2012). Gravity waves mapped by the OMEGA/MEX instrument through O_2 dayglow at 1.27 μm: Data analysis and atmospheric modeling. *Journal of Geophysical Research*, *117*(E11), E00J08. https://doi.org/10.1029/2012JE004065

Angelats i Coll, M., Forget, F., López-Valverde, M., & González-Galindo, F. (2005). The first Mars thermospheric general circulation model: The Martian atmosphere from the ground to 240 km. *Geophysical Research Letters*, *32*(4), L4201. https://doi.org/10.1029/2004GL021368

Benna, M., Bougher, S., Lee, Y., Roeten, K., Yiğit, E., Mahaffy, P., & Jakosky, B. (2019). Global circulation of Mars' upper atmosphere. *Science*, *366*(6471), 1363–1366. https://doi.org/10.1126/science.aax1553

Benna, M., & Lyness, E. (2014). MAVEN neutral gas and ion mass spectrometer data [Dataset]. NASA Planetary Data System. https://doi.org/10.17189/1518931

Creasey, J. E., Forbes, J. M., & Hinson, D. P. (2006). Global and seasonal distribution of gravity wave activity in Mars' lower atmosphere derived from MGS radio occultation data. *Geophysical Research Letters*, *33*(1), L01803. https://doi.org/10.1029/2005GL024037

Creasey, J. E., Forbes, J. M., & Keating, G. M. (2006). Density variability at scales typical of gravity waves observed in Mars' thermosphere by the MGS accelerometer. *Geophysical Research Letters*, *33*(22), L22814. https://doi.org/10.1029/2006GL027583

De la Cámara, A., Lott, F., & Hertzog, A. (2014). Intermittency in a stochastic parameterization of nonorographic gravity waves. *Journal of Geophysical Research: Atmospheres*, *119*(21), 11–905. https://doi.org/10.1002/2014JD022002

Eckermann, S. D. (2011). Explicitly stochastic parameterization of nonorographic gravity wave drag. *Journal of the Atmospheric Sciences*, *68*(8), 1749–1765. https://doi.org/10.1175/2011JAS3684.1

Eliassen, A., & Palm, E. (1960). On the transfer of energy in stationary mountain waves. *Geophysics Publication*, *22*, 1–23.

England, S. L., Liu, G., Yiğit, E., Mahaffy, P. R., Elrod, M., Benna, M., et al. (2017). MAVEN NGIMS observations of atmospheric gravity waves in the Martian thermosphere. *Journal of Geophysical Research: Space Physics*, *122*(2), 2310–2335. https://doi.org/10.1002/2016JA023475

Ferri, F., Karatekin, Ö., Lewis, S. R., Forget, F., Aboudan, A., Colombatti, G., et al. (2019). Exomars atmospheric Mars entry and landing investigations and analysis (AMELIA). *Space Science Reviews*, *215*(1), 1–21. https://doi.org/10.1007/s11214-019-0578-x

Forget, F., Hourdin, F., Fournier, R., Hourdin, C., Talagrand, O., Collins, M., et al. (1999). Improved general circulation models of the Martian atmosphere from the surface to above 80 km. *Journal of Geophysical Research*, *104*(E10), 24155–24175. https://doi.org/10.1029/1999JE001025

Forget, F., Montmessin, F., Bertaux, J.-L., González-Galindo, F., Lebonnois, S., Quemerais, E., et al. (2009). Density and temperatures of the upper Martian atmosphere measured by stellar occultations with Mars Express SPICAM. *Journal of Geophysical Research*, *114*(E1), E01004. https://doi.org/10.1029/2008JE003086

Fritts, D. C. (1984). Gravity wave saturation in the middle atmosphere: A review of theory and observations. *Reviews of Geophysics*, *22*(3), 275–308. https://doi.org/10.1029/RG022i003p00275

Fritts, D. C., Wang, L., & Tolson, R. H. (2006). Mean and gravity wave structures and variability in the Mars upper atmosphere inferred from Mars Global Surveyor and Mars Odyssey aerobraking densities. *Journal of Geophysical Research*, *111*(A12), A12304. https://doi.org/10.1029/2006JA011897

Gilli, G., Forget, F., Spiga, A., Navarro, T., Millour, E., Montabone, L., et al. (2020). Impact of gravity waves on the middle atmosphere of Mars: A non-orographic gravity wave parameterization based on global climate modeling and MCS observations. *Journal of Geophysical Research: Planets*, *125*(3), e2018JE005873. https://doi.org/10.1029/2018JE005873

Gilli, G., Lebonnois, S., González-Galindo, F., López-Valverde, M. A., Stolzenbach, A., Lefèvre, F., et al. (2017). Thermal structure of the upper atmosphere of Venus simulated by a ground-to-thermosphere GCM. *Icarus*, *281*, 55–72. https://doi.org/10.1016/j.icarus.2016.09.016

González-Galindo, F., Forget, F., López-Valverde, M., & Angelats i Coll, M. (2009). A ground-to-exosphere Martian general circulation model: 2. Atmosphere during solstice conditions—Thermospheric polar warming. *Journal of Geophysical Research*, *114*(E8), E08004. https://doi.org/10.1029/2008JE003277

Heavens, N. G., Kass, D. M., Kleinböhl, A., & Schofield, J. T. (2020). A multiannual record of gravity wave activity in Mars's lower atmosphere from on-planet observations by the Mars Climate Sounder. *Icarus*, *341*, 113630. https://doi.org/10.1016/j.icarus.2020.113630

Hines, C. O. (1997). Doppler-spread parameterization of gravity-wave momentum deposition in the middle atmosphere. Part 2: Broad and quasi monochromatic spectra, and implementation. *Journal of Atmospheric and Solar-Terrestrial Physics*, *59*(4), 387–400. https://doi.org/10.1016/S1364-6826(96)00080-6

Hourdin, F., Rio, C., Grandpeix, J.-Y., Madeleine, J.-B., Cheruy, F., Rochetin, N., et al. (2020). LMDZ6A: The atmospheric component of the IPSL climate model with improved and better tuned physics. *Journal of Advances in Modeling Earth Systems*, *12*(7), e2019MS001892. https://doi.org/10.1029/2019MS001892

Jakosky, B. M., & Martin, T. Z. (1987). Mars: North-polar atmospheric warming during dust storms. *Icarus*, *72*(3), 528–534. https://doi.org/10.1016/0019-1035(87)90050-9

Kleinböhl, A., Friedson, A. J., & Schofield, J. T. (2017). Two-dimensional radiative transfer for the retrieval of limb emission measurements in the Martian atmosphere. *Journal of Quantitative Spectroscopy and Radiative Transfer*, *187*, 511–522. https://doi.org/10.1016/j.jqsrt.2016.07.009

Kleinböhl, A., Schofield, J. T., Kass, D. M., Abdou, W. A., Backus, C. R., Sen, B., et al. (2009). Mars Climate Sounder limb profile retrieval of atmospheric temperature, pressure, and dust and water ice opacity. *Journal of Geophysical Research*, *114*(E10), E10006. https://doi.org/10.1029/2009JE003358

Kuroda, T., Medvedev, A. S., & Yiğit, E. (2020). Gravity wave activity in the atmosphere of Mars during the 2018 global dust storm: Simulations with a high-resolution model. *Journal of Geophysical Research: Planets*, *125*(11), e2020JE006556. https://doi.org/10.1029/2020JE006556

Kuroda, T., Medvedev, A. S., Yiğit, E., & Hartogh, P. (2016). Global distribution of gravity wave sources and fields in the Martian atmosphere during equinox and solstice inferred from a high-resolution general circulation model. *Journal of the Atmospheric Sciences*, *73*(12), 4895–4909. https://doi.org/10.1175/JAS-D-16-0142.1

Lee, C., Lawson, W., Richardson, M., Heavens, N., Kleinböhl, A., Banfield, D., et al. (2009). Thermal tides in the Martian middle atmosphere as seen by the Mars Climate Sounder. *Journal of Geophysical Research*, *114*(E3), E03005. https://doi.org/10.1029/2008JE003285

Li, Y., Liu, J., & Jin, S. (2021). Horizontal internal gravity waves in the Mars upper atmosphere from MAVEN ACC and NGIMS measurements. *Journal of Geophysical Research: Space Physics*, *126*(1), e2020JA028378. https://doi.org/10.1029/2020JA028378

Lindzen, R. S. (1981). Turbulence and stress owing to gravity wave and tidal breakdown. *Journal of Geophysical Research*, *86*(C10), 9707–9714. https://doi.org/10.1029/JC086iC10p09707

Liu, J., Jin, S., & Li, Y. (2019). Seasonal variations and global wave distributions in the Mars thermosphere from MAVEN and multi-satellites accelerometer-derived mass densities. *Journal of Geophysical Research: Space Physics*, *124*(11), 9315–9334. https://doi.org/10.1029/2019JA026720

Liu, J., Montabone, L., & Millour, E. (2023). Data for A Surface to exosphere non-orographic gravity wave parameterization for the Mars planetary climate model [Dataset]. Mendeley Data. https://doi.org/10.17632/b98dt7f4db.1

Lott, F., & Guez, L. (2013). A stochastic parameterization of the gravity waves due to convection and its impact on the equatorial stratosphere. *Journal of Geophysical Research: Atmospheres*, *118*(16), 8897–8909. https://doi.org/10.1002/jgrd.50705

Lott, F., Guez, L., & Maury, P. (2012). A stochastic parameterization of non-orographic gravity waves: Formalism and impact on the equatorial stratosphere. *Geophysical Research Letters*, *39*(6), L06807. https://doi.org/10.1029/2012GL051001

Lott, F., & Miller, M. J. (1997). A new subgrid-scale orographic drag parametrization: Its formulation and testing. *Quarterly Journal of the Royal Meteorological Society*, *123*(537), 101–127. https://doi.org/10.1002/qj.49712353704

Mahaffy, P. R., Benna, M., Elrod, M., Yelle, R. V., Bougher, S. W., Stone, S. W., & Jakosky, B. M. (2015a). Structure and composition of the neutral upper atmosphere of Mars from the MAVEN NGIMS investigation. *Geophysical Research Letters*, *42*(21), 8951–8957. https://doi.org/10.1002/2015GL065329

Mahaffy, P. R., Benna, M., King, T., Harpold, D. N., Arvey, R., Barciniak, M., et al. (2015b). The neutral gas and ion mass spectrometer on the Mars atmosphere and volatile evolution mission. *Space Science Reviews*, *195*(1), 49–73. https://doi.org/10.1007/s11214-014-0091-1

Manzini, E., McFarlane, N. A., & McLandress, C. (1997). Impact of the Doppler spread parameterization on the simulation of the middle atmosphere circulation using the MA/ECHAM4 general circulation model. *Journal of Geophysical Research*, *102*(D22), 25751–25762. https://doi.org/10.1029/97JD01096

McCleese, D. J., Heavens, N., Schofield, J., Abdou, W., Bandfield, J., Calcutt, S., et al. (2010). Structure and dynamics of the Martian lower and middle atmosphere as observed by the Mars Climate Sounder: Seasonal variations in zonal mean temperature, dust, and water ice aerosols. *Journal of Geophysical Research*, *115*(E12), E05S06. https://doi.org/10.1029/2010JE003677

McCleese, D. J., & Schofield, J. T. (2008). MRO Mars climate sounder derived data records V1.0. NASA planetary data system [Dataset]. NASA Planetary Data System. https://doi.org/10.17189/P73K-XY37

McCleese, D. J., Schofield, J., Taylor, F., Abdou, W., Aharonson, O., Banfield, D., et al. (2008). Intense polar temperature inversion in the middle atmosphere on Mars. *Nature Geoscience*, *1*(11), 745–749. https://doi.org/10.1038/ngeo332

McCleese, D. J., Schofield, J., Taylor, F., Calcutt, S., Foote, M., Kass, D., et al. (2007). Mars Climate Sounder: An investigation of thermal and water vapor structure, dust and condensate distributions in the atmosphere, and energy balance of the polar regions. *Journal of Geophysical Research*, *112*(E5), E12016. https://doi.org/10.1029/2006JE002790

Medvedev, A. S., & Yiğit, E. (2012). Thermal effects of internal gravity waves in the Martian upper atmosphere. *Geophysical Research Letters*, *39*(5), L05201. https://doi.org/10.1029/2012GL050852

Medvedev, A. S., Yiğit, E., & Hartogh, P. (2011). Estimates of gravity wave drag on Mars: Indication of a possible lower thermospheric wind reversal. *Icarus*, *211*(1), 909–912. https://doi.org/10.1016/j.icarus.2010.10.013

Miyoshi, Y., Forbes, J., & Moudden, Y. (2011). A new perspective on gravity waves in the Martian atmosphere: Sources and features. *Journal of Geophysical Research*, *116*(E9), E09009. https://doi.org/10.1029/2011JE003800

Montabone, L., Forget, F., Millour, E., Wilson, R., Lewis, S., Cantor, B., et al. (2015). Eight-year climatology of dust optical depth on Mars. *Icarus*, *251*, 65–95. https://doi.org/10.1016/j.icarus.2014.12.034

Montabone, L., Spiga, A., Kass, D. M., Kleinböhl, A., Forget, F., & Millour, E. (2020). Martian year 34 column dust climatology from Mars climate sounder observations: Reconstructed maps and model simulations. *Journal of Geophysical Research: Planets*, *125*(8), e2019JE006111. https://doi.org/10.1029/2019JE006111

Nakagawa, H., Terada, N., Jain, S. K., Schneider, N. M., Montmessin, F., Yelle, R. V., et al. (2020). Vertical propagation of wave perturbations in the middle atmosphere on Mars by MAVEN/IUVS. *Journal of Geophysical Research: Planets*, *125*(9), e2020JE006481. https://doi.org/10.1029/2020JE006481

Petrosyan, A., Galperin, B., Larsen, S. E., Lewis, S., Määttänen, A., Read, P., et al. (2011). The Martian atmospheric boundary layer. *Reviews of Geophysics*, *49*(3), RG3005. https://doi.org/10.1029/2010RG000351

Pottier, A., Forget, F., Montmessin, F., Navarro, T., Spiga, A., Millour, E., et al. (2017). Unraveling the Martian water cycle with high-resolution global climate simulations. *Icarus*, *291*, 82–106. https://doi.org/10.1016/j.icarus.2017.02.016

Roeten, K., Bougher, S., Yigit, E., Medvedev, A., Benna, M., & Elrod, M. (2022). Impacts of gravity waves in the Martian thermosphere: The Mars Global Ionosphere-Thermosphere Model coupled with a whole atmosphere gravity wave scheme. *Journal of Geophysical Research: Planets*, *127*(12), e2022JE007477. https://doi.org/10.1029/2022JE007477

Siddle, A., Mueller-Wodarg, I., Stone, S., & Yelle, R. (2019). Global characteristics of gravity waves in the upper atmosphere of Mars as measured by MAVEN/NGIMS. *Icarus*, *333*, 12–21. https://doi.org/10.1016/j.icarus.2019.05.021

Smith, M. D., Pearl, J. C., Conrath, B. J., & Christensen, P. R. (2001). Thermal emission spectrometer results: Mars atmospheric thermal structure and aerosol distribution. *Journal of Geophysical Research*, *106*(E10), 23929–23945. https://doi.org/10.1029/2000JE001321

Spiga, A., González-Galindo, F., López-Valverde, M.-Á., & Forget, F. (2012). Gravity waves, cold pockets and CO_2 clouds in the Martian mesosphere. *Geophysical Research Letters*, *39*(2), L02201. https://doi.org/10.1029/2011GL050343

Starichenko, E. D., Belyaev, D. A., Medvedev, A. S., Fedorova, A. A., Korablev, O. I., Trokhimovskiy, A., et al. (2021). Gravity wave activity in the Martian atmosphere at altitudes 20–160 km from ACS/TGO occultation measurements. *Journal of Geophysical Research: Planets*, *126*(8), e2021JE006899. https://doi.org/10.1029/2021JE006899

Stone, S. W., Yelle, R. V., Benna, M., Elrod, M. K., & Mahaffy, P. R. (2018). Thermal structure of the Martian upper atmosphere from MAVEN NGIMS. *Journal of Geophysical Research: Planets*, *123*(11), 2842–2867. https://doi.org/10.1029/2018JE005559

Tellmann, S., Pätzold, M., Häusler, B., Hinson, D., & Tyler, G. L. (2013). The structure of Mars lower atmosphere from Mars Express Radio Science (MaRS) occultation measurements. *Journal of Geophysical Research: Planets*, *118*(2), 306–320. https://doi.org/10.1002/jgre.20058

Terada, N., Leblanc, F., Nakagawa, H., Medvedev, A. S., Yiğit, E., Kuroda, T., et al. (2017). Global distribution and parameter dependences of gravity wave activity in the Martian upper thermosphere derived from MAVEN/NGIMS observations. *Journal of Geophysical Research: Space Physics*, *122*(2), 2374–2397. https://doi.org/10.1002/2016JA023476

Vals, M., Spiga, A., Forget, F., Millour, E., Montabone, L., & Lott, F. (2019). Study of gravity waves distribution and propagation in the thermosphere of Mars based on MGS, ODY, MRO and MAVEN density measurements. *Planetary and Space Science*, *178*, 104708. https://doi.org/10.1016/j.pss.2019.104708

Warner, C., & McIntyre, M. (1996). On the propagation and dissipation of gravity wave spectra through a realistic middle atmosphere. *Journal of the Atmospheric Sciences*, *53*(22), 3213–3235. https://doi.org/10.1175/1520-0469(1996)053⟨3213:OTPADO⟩2.0.CO;2

Warner, C., & McIntyre, M. (2001). An ultrasimple spectral parameterization for nonorographic gravity waves. *Journal of the Atmospheric Sciences*, *58*(14), 1837–1857. https://doi.org/10.1175/1520-0469(2001)058⟨1837:AUSPFN⟩2.0.CO;2

Wilson, R. J. (1997). A general circulation model simulation of the Martian polar warming. *Geophysical Research Letters*, *24*(2), 123–126. https://doi.org/10.1029/96GL03814

Wright, C. J. (2012). A one-year seasonal analysis of Martian gravity waves using MCS data. *Icarus*, *219*(1), 274–282. https://doi.org/10.1016/j.icarus.2012.03.004

Yiğit, E., Aylward, A. D., & Medvedev, A. S. (2008). Parameterization of the effects of vertically propagating gravity waves for thermosphere general circulation models: Sensitivity study. *Journal of Geophysical Research*, *113*(D19), D19106. https://doi.org/10.1029/2008JD010135

Yiğit, E., England, S. L., Liu, G., Medvedev, A. S., Mahaffy, P. R., Kuroda, T., & Jakosky, B. M. (2015). High-altitude gravity waves in the Martian thermosphere observed by MAVEN/NGIMS and modeled by a gravity wave scheme. *Geophysical Research Letters*, *42*(21), 8993–9000. https://doi.org/10.1002/2015GL065307

Yiğit, E., & Medvedev, A. S. (2017). Influence of parameterized small-scale gravity waves on the migrating diurnal tide in Earth's thermosphere. *Journal of Geophysical Research: Space Physics*, *122*(4), 4846–4864. https://doi.org/10.1002/2017JA024089

Yiğit, E., Medvedev, A. S., Benna, M., & Jakosky, B. M. (2021). Dust storm-enhanced gravity wave activity in the Martian thermosphere observed by MAVEN and implication for atmospheric escape. *Geophysical Research Letters*, *48*(5), e2020GL092095. https://doi.org/10.1029/2020GL092095